DROP-IT

DELIVERABLE 1.2

Obtaining B-LFP nanocrystals and properties

Due date of deliverable: 2020/10/31

Actual submission date: 2020/12/21

Deliverable number:	D1.2
Due date:	31.10.2020
Nature[1]:	R
Dissemination Level[1]:	PU
Work Package:	WP1
Lead Beneficiary:	ETH Zürich
Contributing Beneficiaries:	ETHZ, AVA, UJI

[1] **Nature:** R = Report, P = Prototype, D = Demonstrator, O = Other
Dissemination level PU = Public PP = Restricted to other programme participants (including the Commission Services) RE = Restricted to a group specified by the consortium (including the Commission Services) CO = Confidential, only for members of the consortium (including the Commission Services) Restraint UE = Classified with the classification level "Restraint UE" according to Commission Deci-sion 2001/844 and amendments Confidential UE = Classified with the mention of the classification level "Confidential UE" according to Commission Decision 2001/844 and amendments Secret UE = Classified with the mention of the classification level "Secret UE" according to Commis-sion Decision 2001/844 and amendments

This project has received funding from the European Union's Horizon 2020 research and innovation programme under **Grant Agreement No. 862656**.

DOCUMENT HISTORY

Version	*Date*	*Reason of change*
1	2020/11/18	Contribution from ETHZ
2	2020/11/30	Contribution from UJI
3	2020/12/04	Contribution from Avantama
4	2020/12/08	Contribution from ETHZ
5	2020/12/15	Contribution from ETHZ
6	2020/12/16	Revision by all contributors

This project has received funding from the European Union's Horizon 2020 research and innovation programme under **Grant Agreement No. 862656**.

Table of Content

This project has received funding from the European Union's Horizon 2020 research and innovation programme under **Grant Agreement No. 862656**.

1 Introduction

Deliverable number	Deliverable title	WP number	Lead beneficiary	Due Date (in months)	Description
D1.2	Obtaining B-LFP nanocrystals and properties	WP1	ETH Zürich	12	B-LFP (Sn-based) Nanocrystals will be synthesized and their main optical and structural properties will be analyzed. A suitable surface passivation will be developed for achieving long-term stability of optoelectronic/photonic devices.

2 Description of work & main achievements

LFP materials investigated in WP1 naturally split in two families: $FASnI_3$ LFP with three-dimensional lattice and all other materials with lower dimensionality. In case of photovoltaics, the requirement for the nearly ideal 3D perovskite structure narrows the list of perspective materials down to tin (II) and germanium (II) iodide AMI_3 perovskites where A is either methylammonium, cesium, formamidinium or their mixtures. Materials with lower dimensionality are mainly considered for other applications, such as broad-band photoluminescence, photodetection, etc.

The most recent reports have shown that optimal corner-sharing connectivity between metal halide polyhedra and metal-iodide-metal bond of about 180° are essential for efficient band dispersion and low effective mass of carriers. Optimal connection of the polyhedra ensures the high overlap of p-orbitals for metal and halide atoms. This topic is discussed in more details in the report on Deliverable 1.1. Among all known LFP materials, only $ASnI_3$ and $AGeI_3$ (A=Cs, methylammonium or FA) enable optimal connectivity between metal iodide octahedra and metal-iodide-metal bond of about 180°. The main issue with these compounds is their low oxidative stability since Sn^{2+} and Ge^{2+} are prone to oxidation to the 4+ state. The most stable one out of these six compounds is $FASnI_3$. Recent literature shows that special care about proper processing and encapsulation of $FASnI_3$ photovoltaic cells allows achieving power conversion efficiency as high as 13 %. This motivated us to consider this material as a benchmark for LFP halide perovskite photovoltaics. Accordingly, a colloidal synthesis of $FASnI_3$ NCs with nearly the best possible morphological quality and purity has been developed. This method allows synthesis of highly monodisperse $FASnI_3$ NCs with size of about 10 nm and without any detectable impurities of other phases. Furthermore, we have shown that optical properties of these NCs are not limited by the expected presence of Sn^{4+} states. Instead, these NCs exhibit structure which is slightly different from the structure of bulk $FASnI_3$: disorder of the I-sites reduces Sn-I-Sn angle and slightly opens the bandgap. Based on this finding, a pathway for tuning the optical properties via altering crystal lattice has been suggested and achieved by doping $FASnI_3$ with ethylenediammonium. Obtained $FASnI_3$ NCs require air-free storage and processing conditions. In nitrogen-filled glovebox solutions of $FASnI_3$ NCs are stable for at least several weeks, whereas being exposed to air they oxidize on an hour-scale.

An alternative LFP materials have been explored for other fields of optoelectronics. This includes doped double perovskites and CsBr, vacancy-ordered double perovskites, rudorfites, and $Cs_3Bi_2I_9$ nanocrystals. These materials may be potentially interesting from several perspectives with two most

important: as broadband emitters and as photoconductors. Some of these materials (Sn-doped double perovskites and Sn-doped CsBr) exhibit broadband photoluminescence in visible range. This photoluminescence originates from the self-trapped exciton states and can reach 20-90 % quantum yield which allows to consider these materials for lightening or remote thermography applications. Other materials (Cs_2SnI_6 and $Cs_3Bi_2I_9$) potentially can be interesting for photodetection. Although these materials unlikely can exhibit conductivity and light absorption comparable to lead halide perovskites, they at the same time potentially can exhibit significantly lower dark current if lower number of defects and ionic conductivity are achieved. This may allow to achieve photoconductivity which is comparable to the lead halide perovskites, similarly as it has been down earlier for $Cs_2AgBiBr_6$ double LFP material.

3 Results

3.1 Benchmark $FASnI_3$ colloidal nanocrystals by hot-injection method

3.1.1 Development of the synthesis of colloidal $FASnI_3$ NCs

Various synthetic approaches to the synthesis of colloidal $FASnI_3$ NCs have been tested. This includes screening the precursors suitable for the hot-injection reaction pathway, searching for optimal ligands, solvents, concentrations, injection and growth temperatures, and growth time.

3.1.1.1 Synthesis in 1-octadecene (ODE). Issue with ODE.

The first set of optimal conditions have been discovered for 1-octadecene as a solvent. This synthesis allows for obtaining monodisperse $FASnI_3$ NCs, which was a primary goal of this work (Figure 3.1.1-1). However, it has been found that a combination of 1-octadecene, oleylamine, and SnI_2 in a given synthetic conditions leads to the oxidation of iodide anions to polyiodide ones. Such oxidation is a unique feature of this system and is likely catalyzed by SnI_2.

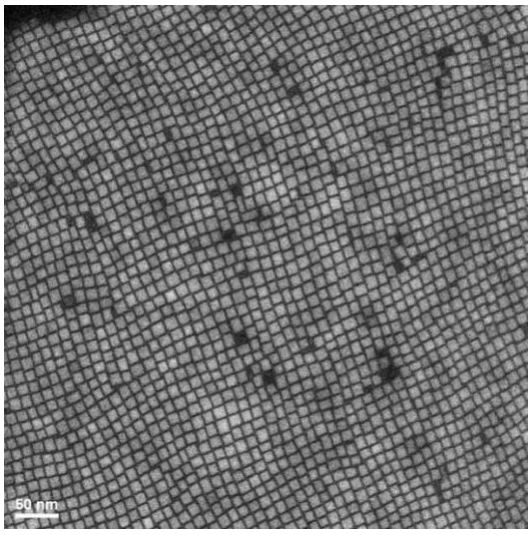

Figure 3.1.1-1. Dark field STEM image of the representative FASnI3 NCs sample synthesized in ODE.

The presence of polyiodides is reported to be beneficial in case of lead halide perovskites, where polyiodides can oxidize metallic lead to Pb^{2+} state but not further. However, in case of tin halide perovskites the presence of polyiodides is potentially an issue not only because they absorb light in the visible range but also because they can oxidize Sn^{2+} to Sn^{4+} as their reduction potential is higher than that of Sn^{4+} (Table 3.1.1-1).

Table 3.1.1-1. Reduction potentials polyiodide in comparison with other relevant species.

Reduction reaction	Standard reduction potential, V
$Pb^{2+} + 2e^- \rightarrow Pb^0$	~-0.4
$Sn^{2+} + 2e^- \rightarrow Sn^0$	~-0.13
$Sn^{4+} + 2e^- \rightarrow Sn^{2+}$	~+0.15
$I_3^- + 2e^- \rightarrow 3I^-$	~+0.53
$Pb^{4+} + 2e^- \rightarrow Pb^{2+}$	~+1.69

In order to check the possible reasons for the oxidation of iodide anions to polyiodides, the purity of all precursors has been checked first.

3.1.1.2 Purity of the precursors

Experimentally, it has been found that SnI_2 supplied by Strem exhibits the best performance in our synthetic protocol. However, available purity has been insufficient even in this case as this SnI_2 was not completely soluble in the reaction mixture, producing slightly scattering solution instead. In order to exclude possible effects of the impurities on the oxidation of iodide and also to ensure homogeneous nucleation of $FASnI_3$ NCs, we have additionally purified commercial SnI_2 by sublimation in ultrahigh vacuum (Figure 3.1.1-2). Powder purified by sublimation was completely soluble in the reaction conditions and allowed the synthesis of monodisperse $FASnI_3$ NCs.

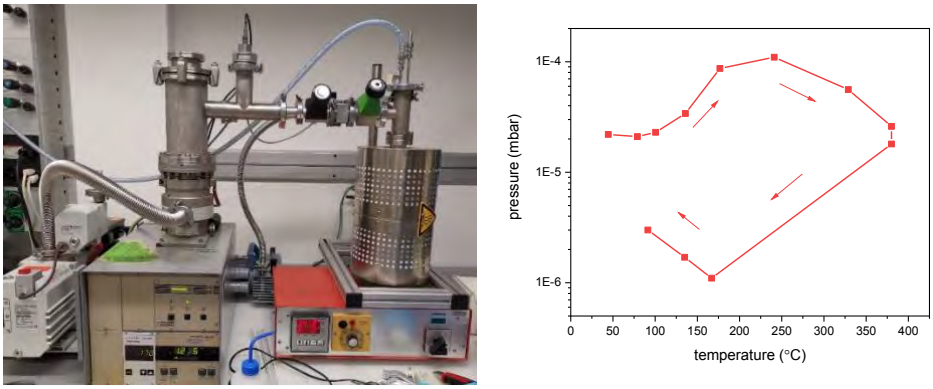

Figure 3.1.1-2. Setup and temperature-pressure profile for the purification of SnI_2 by sublimation in ultrahigh vacuum.

All liquid components involved in the synthesis (solvents and ligands) have been either distilled or dried under high vacuum in order to exclude the potential effect of impurities on the oxidation of iodide anions. For example, utilized oleylamine has 95 % purity and therefore has been distilled.

Despite all these precautions, oxidation of the iodide to polyiodide has remained and was found to be driven by the mutual reaction of ODE, OLAm, SnI_2 at elevated temperature (80 °C). because of that, other solvents have been tested for the reaction in otherwise analogous conditions.

3.1.1.3 Synthesis in aromatic solvents.

Three potentially suitable aromatic solvents have been chosen as a replacement for 1-octadecene: toluene, mesitylene, and eutectic mixture of diphenyl and diphenyl oxide (Dowterm A). Oxidation of iodide anions to polyiodides have not been observed in all three cases. All three solvents allow the synthesis of monodisperse $FASnI_3$ nanocrystals in a temperature range 25-80 °C (Figure 3.1.1-3).

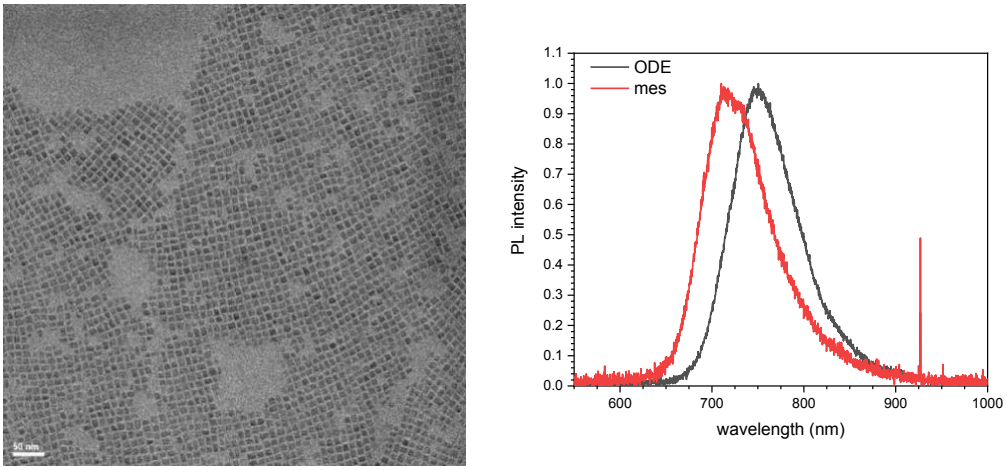

Figure 3.1.1-3. TEM image and PL spectrum of the representative $FASnI_3$ NCs synthesized in mesitylene in comparison with PL spectrum of the sample synthesized in ODE.

However, it has been found that the first two solvents are not optimal for the preparation of one of the precursors, namely formamidinium oleate. According to the developed protocol the solution of formamidinium oleate has to be prepared in advance by drying the mixture of formamidinium acetate and oleic acid under vacuum at elevated temperatures. Although synthesis of formamidinium oleate under low vacuum (0.2-0.5 bar) and mild heating (80 °C) is possible, the byproduct – acetic acid – cannot be completely removed from the solution in these conditions. Acetic acid can affect the reaction analogously to oleic acid and therefore, uncontrolled amount of the acetic acid reduces the reproducibility of the synthetic protocol and also the stability of the synthesized $FASnI_3$ NCs. In contrast, synthesis of formamidinium oleate in high boiling point Dowtherm A solvent allows complete removal of the acetic acid at higher vacuum (~10^{-2} mbar, 80 °C). Therefore, Dowtherm A has been identified as the most promising solvent for the developed synthetic approach and further optimization of the protocol has been performed with this solvent.

3.1.1.4 Synthesis in high boiling point aromatic solvent. Optimization of the synthetic conditions. Morphological quality of the obtained $FASnI_3$ NCs.

Synthesis of $FASnI_3$ NCs in stoichiometric conditions results in polydisperse samples (Figure 3.1.1-4). Moderate (2:1) excess of Sn in respect to FA significantly improves monodispersity of the obtained NCs. Even higher Sn:FA ratio results in samples with slightly brighter photoluminescence but at the same time favours formation of the mixture of nanocrystals and nanoplatelets and therefore again increases the polydispersity of the sample.

Synthesis requires combination of trioctylphosphine, oleic acid and oleylamine as ligands (Figure 3.1.1-5). Synthesis performed without trioctylphosphine results in a mixture of bulk $FASnI_3$ material and nanowires. Synthesis performed without oleylamine results in rather large $FASnI_3$ NCs of about 200 nm in size.

Altering amount of the oleic acid affects only polydispersity of NCs with minimum amount of oleic acid promoting more monodisperse NCs (Figure 3.1.1-6).

Variation of the injection and growth temperature in range from 40 to 110 °C does not affect the product significantly (Figure 3.1.1-7). Further increase of the injection temperature to 120 °C results in bulk sample.

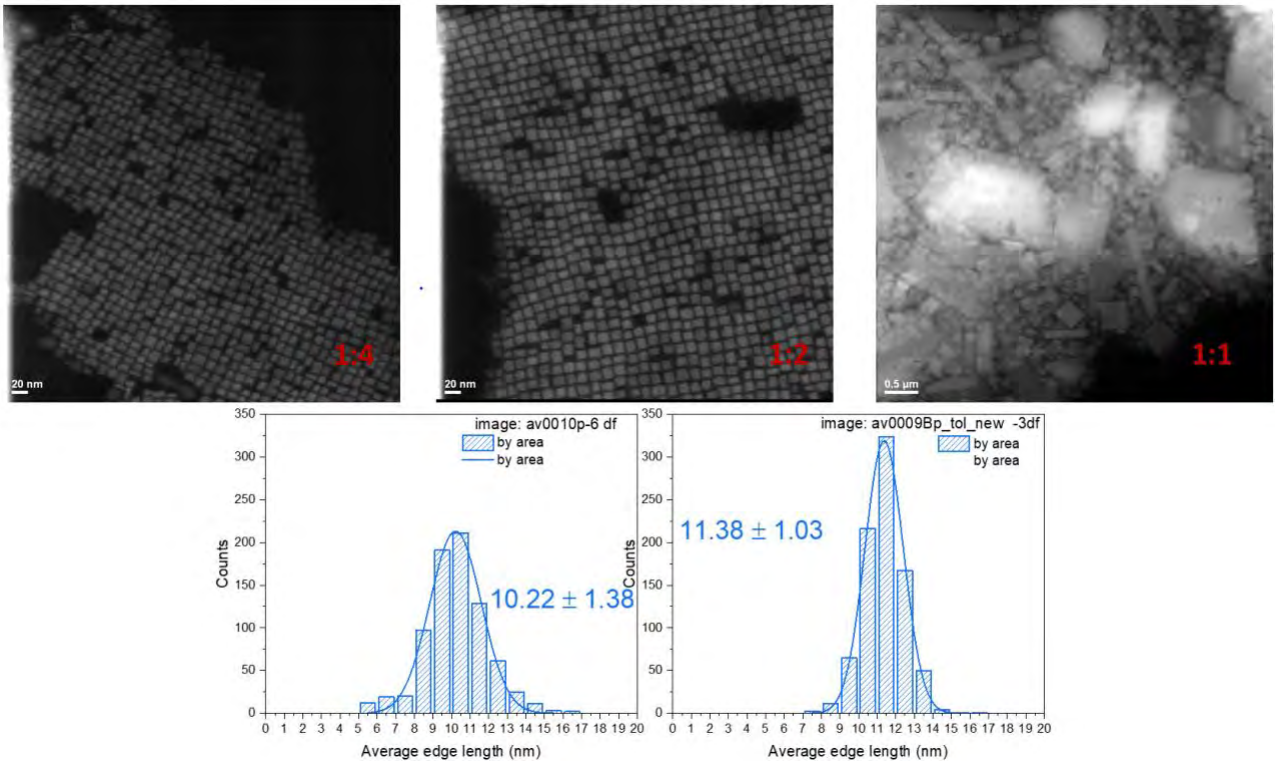

Figure 3.1.1-4. Dark field STEM images and size histograms for the $FASnI_3$ NCs synthesized with FA:Sn ratio 1:4 and 1:2 and TEM image for the sample synthesized with 1:1 stoichiometry.

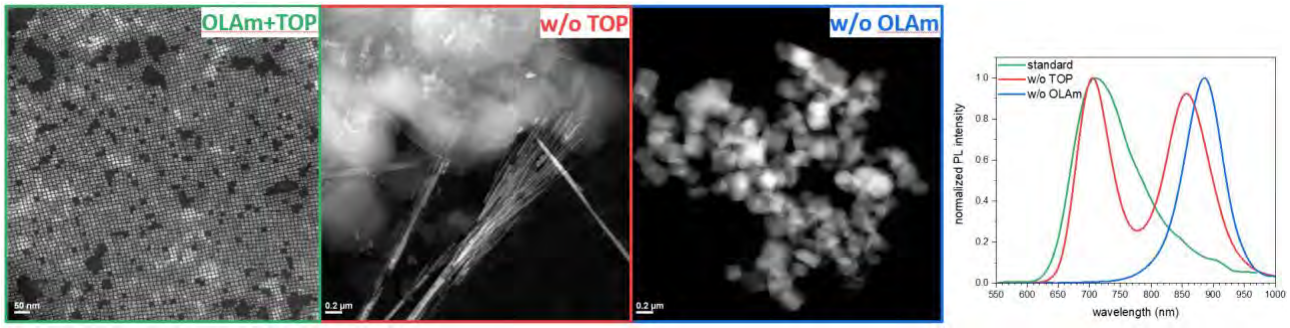

Figure 3.1.1-5. Dark filed STEM images and PL spectra for the $FASnI_3$ NCs synthesized with all three ligands (oleic acid, oleylamine and trioctylphosphine) and in the absence of either trioctylphosphine or oleylamine.

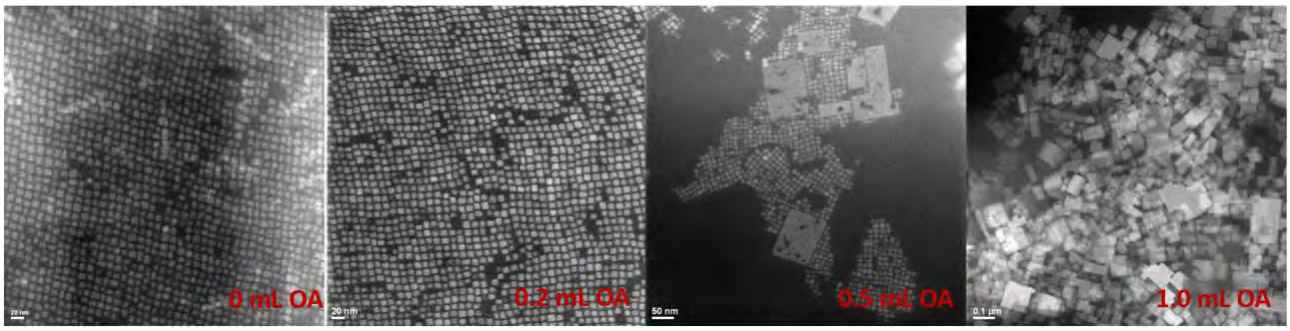

Figure 3.1.1-6. Dark filed STEM images of $FASnI_3$ NCs synthesized with different amounts of oleic acid.

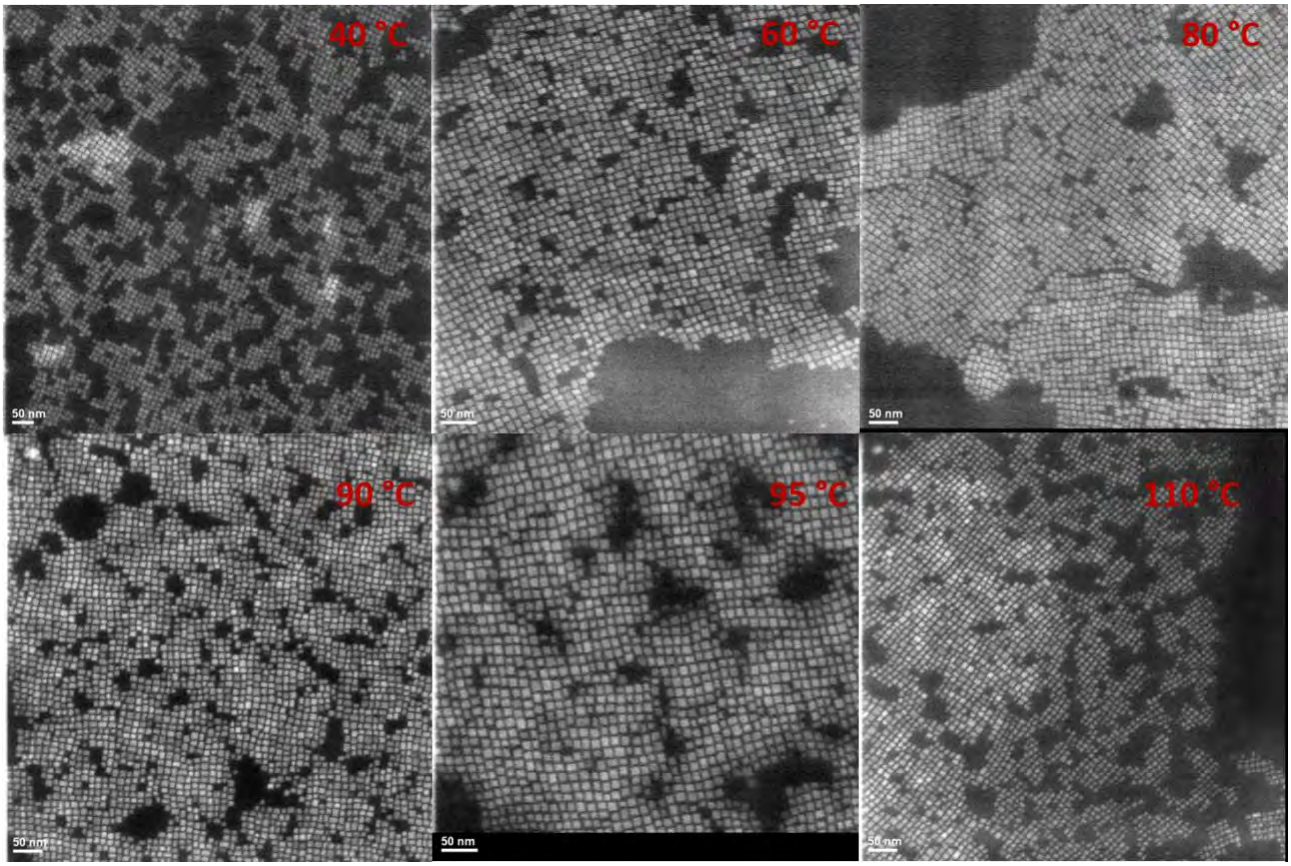

Figure 3.1.1-7. Dark filed STEM images of $FASnI_3$ NCs synthesized at different temperatures in range 40-110 °C.

After optimization of the synthesis temperature, time, ligands, and FA:Sn ratio, optimal synthetic conditions have been identified. Synthesis in Dowtherm A, with oleylamine, oleic acid, and trioctylphosphine as ligands, FA:Sn 2:1 ratio and temperature in the range 25-110 °C allows highly monodisperse $FASnI_3$ NCs (Figure 1.3.1-8).

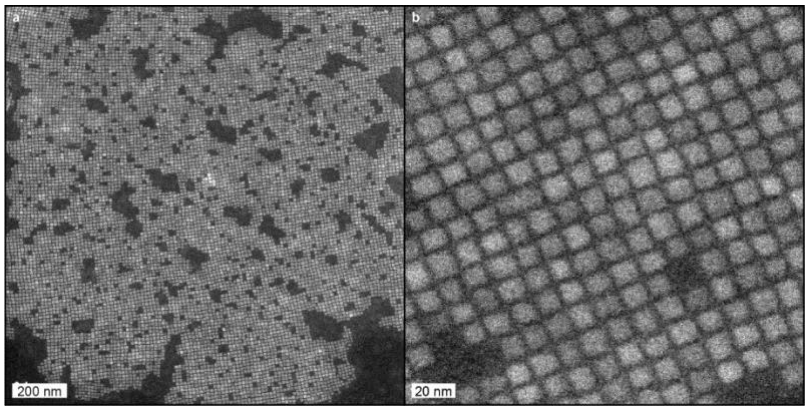

Figure 3.1.1-8. Low (a) and high (b) magnification dark filed STEM images of $FASnI_3$ NCs synthesized in fully optimized synthetic conditions at 80 °C.

3.1.2 Washing protocol.

XRD of the obtained $FASnI_3$ NCs indicated that such samples contain large amount of byproducts. Therefore, an additional washing protocol has been developed. For this NCs has been precipitated from colloidal solution by various amount of antisolvents. Precipitate has been redissolved in the solvent and only soluble fraction has been used for further characterization. Hexane, chloroform and toluene have been tested as solvents and acetone, acetonitrile and ethyl acetate as antisolvents. Required ratio between solvent and antisolvent varied for specific pairs. An optimal washing has been achieved with acetonitrile as anitisolvent and either toluene or chloroform as solvent. This washing allows to remove all byproducts and minimize the amount of free ligands without compromising monodispersity and stability of $FASnI_3$ NCs.

3.1.3 Optical properties of FASnI3 NCs. Bandgap issue.

Developed colloidal $FASnI_3$ NCs exhibit absorption edge and photoluminescence in the range 710-780 nm (Figure 3.1.2-1). Photoluminescence quantum yield (PL QY) is about 0.2 %. Time-resolved PL decay is found to be nearly wavelength-independent, confirming uniformity of the NCs. PL lifetime is biexponential with average lifetimes of 0.3 ns (90 %) and 1.9 ns (10 %), which is in good agreement with previously reported PL lifetimes for bulk $FASnI_3$.[Nat. Comm. 2018, 9:243]

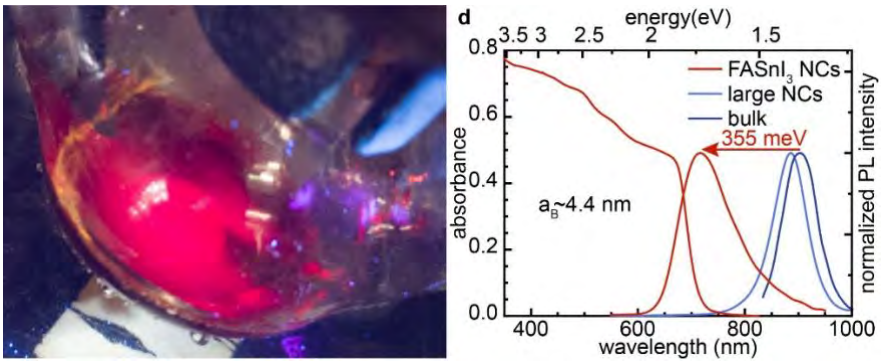

Figure 3.1.3-1: (a) photograph and (b) optical properties of colloidal $FASnI_3$ NCs in comparison with PL of the bulk $FASnI_3$, and PL of large NCs synthesized without oleylamine.

Absorption edge and PL of the synthesized $FASnI_3$ NCs are notably – by 200-355 meV – shifted from the bandgap of bulk $FASnI_3$. Although quantum confinement derived blueshift of the bandgap is expected for colloidal NCs, such a big shift can hardly be explained solely by quantum

confinement. The obtained NCs are about 10 nm large, whereas the predicted exciton Bohr radius is about 4.4 nm only, meaning that these NCs should be in a weak confinement regime.

3.1.4 Phase purity.

After the exclusion of the potential effects of impurities, the possibility of reduced crystallographic symmetry has been considered as a possible origin of the observed blueshift of the bandgap. Bulk $FASnI_3$ crystallizes in cubic perovskite structure at room temperature. The slight distortion of such lattice can potentially lower the symmetry to tetragonal or even orthorhombic structures. Reduced Sn-I-Sn angle, in this case, will reduce overlap of valence orbitals and therefore open the bandgap. This phenomenon is well-known for metal halide perovskite-like compounds.

To check this hypothesis, a thorough XRD study has been performed on powdered and dissolved NCs, on laboratory XRD and XRD with synchrotron light source (PSI, Switzerland; in collaboration with Prof. A. Guagliardi, Italy). The data obtained on SLS XRD indicates that the time-averaged structure of the obtained $FASnI_3$ NCs is undoubtedly cubic. However, detailed modeling of the experimental data shows a high dynamic disorder of I-sites. An analogous phenomenon has been previously observed for methylammonium lead iodide.[Energy Environ. Sci., 2016, 9, 155] In that case, the time-averaged structure is cubic, but the system strongly deviates from such a structure in the sub-picosecond time scale. Thus, on the time scale of electronic transitions, the material experiences a distorted tetragonal environment, reducing the observed bandgap. Reduced symmetry of $FASnI_3$ NCs is also confirmed by solid-state NMR (Figure 1.2-3b).

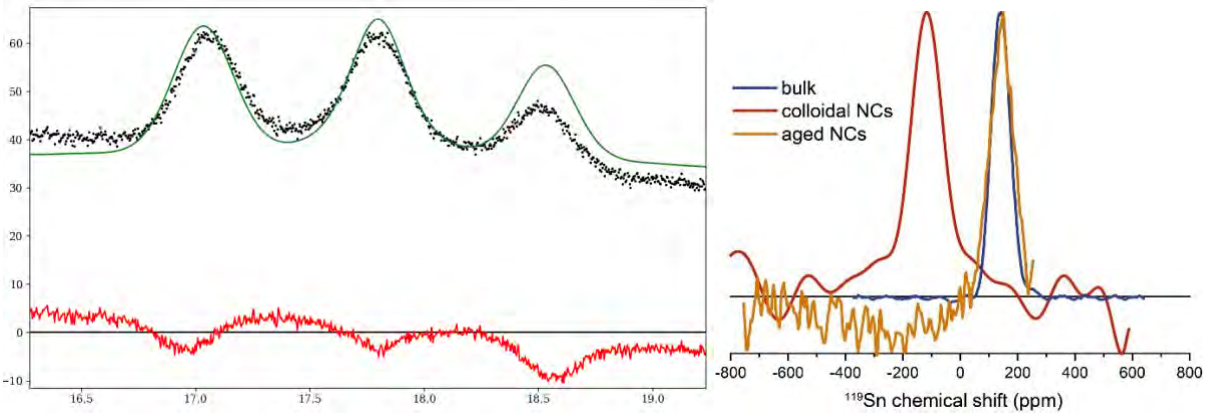

Figure 3.1.4-1. (left) an example of the misfit between SLS XRD and the cubic model structure for $FASnI_3$; (right) solid-state ^{119}Sn NMR data for bulk and colloidal $FASnI_3$.

3.1.5 Oxidative stability of $FASnI_3$ NCs. Impurity of Sn^{4+}. Effect of the reducing agents and antioxidants.

Relatively low PL QY of $FASnI_3$ is commonly associated with partial oxidation of Sn^{2+} to Sn^{4+} introducing trap states within the bandgap. Therefore, a thorough investigation of the effect of various antioxidants and reducing agents on the optical properties of the obtained $FASnI_3$ NCs has been performed. Namely, butylated hydroxytoluene, triethylphosphite, sodium diisooctylphosphinate, lithium aluminium hydride, diborane, sodium borohydride, diisobutylaluminium hydride, tin fluoride and highly selective reducing Mashima's reagent in combination with SnF_2 have been tested either as an additive to the reaction or in postprocessing of the obtained NCs. In all these cases reducing agents either didn't affect the optical properties of $FASnI_3$ NCs (mild reducing agents and/or low

concentration) or entirely reduced Sn^{2+} to metallic Sn (strong reducing agents at higher concentrations). This indicates that PL properties of the obtained $FASnI_3$ NCs are not limited by Sn^{4+} states.

3.1.6 Doping $FASnI_3$ with ethylenediammonium.

The apparent absence of Sn^{4+} trap states and the reduced symmetry of the $FASnI_3$ lattice motivated us to explore the possibility for tuning optical properties by slight distortions of the lattice. For this, doping with ethylenediammonium cation has been performed. Such doping is known to produce so-called “hollow” structures, essentially distorting the lattice of metal halide perovskites. Analogous results have been obtained in the case of doping $FASnI_3$ with ethylenediammonium: slight blueshift of the bandgap, more pronounced excitonic absorption peak, slightly enhanced quantum yield. This study will be continued and extended to other cations which potentially can distort the lattice of $FASnI_3$: hydroxyethylammonium and cesium.

3.2 Synthesis of LFP materials by ball-milling

Ball-milling is a well-known mechanochemical top-down approach to the synthesis of nanoparticles. Until now however, it was not often used in the production of photoactive nanocrystalline materials for photovoltaics or light emission. The reason for that is the relatively high mechanical energy (intensity of milling) required to mill the conventional covalent semiconductors (chalcogenide-based) which typically leads to a large number of defects. For these materials such defects usually introduce deep trap states within the bandgap and therefore harm optical properties of the nanocrystals. However, this is not the case for halide perovskites. These materials consist of the covalently-bound metal halide framework which is balanced by ionically bound alkali or small organic cations. This, together with high ionic mobility, significantly increases the softness of halide perovskites and allows to ball-mill them at rather low energies. Synthesis of LFP bulk and nanomaterials via ball-milling has been developed by Avantama AG.

3.2.1 Synthesis of bulk LFP materials by ball-milling

Bulk Cs_2SnI_6, $FA_3Bi_2Br_9$, Ag_2BiI_5 and Ag_3BiI_6 LFP compounds have been successfully developed and manufactured by Avantama AG via ball milling. The method used hereby offers detailed parameter control (like milling medium and size, temperature, energy), high quality output and non-limited upscale possibilities. The bulk LFP particles produced by ball milling method show high crystallinity and a primary particle size in µm regime. The XRD diffractograms of the synthesized bulk LFPs are depicted in Figure 3.2.1-1.

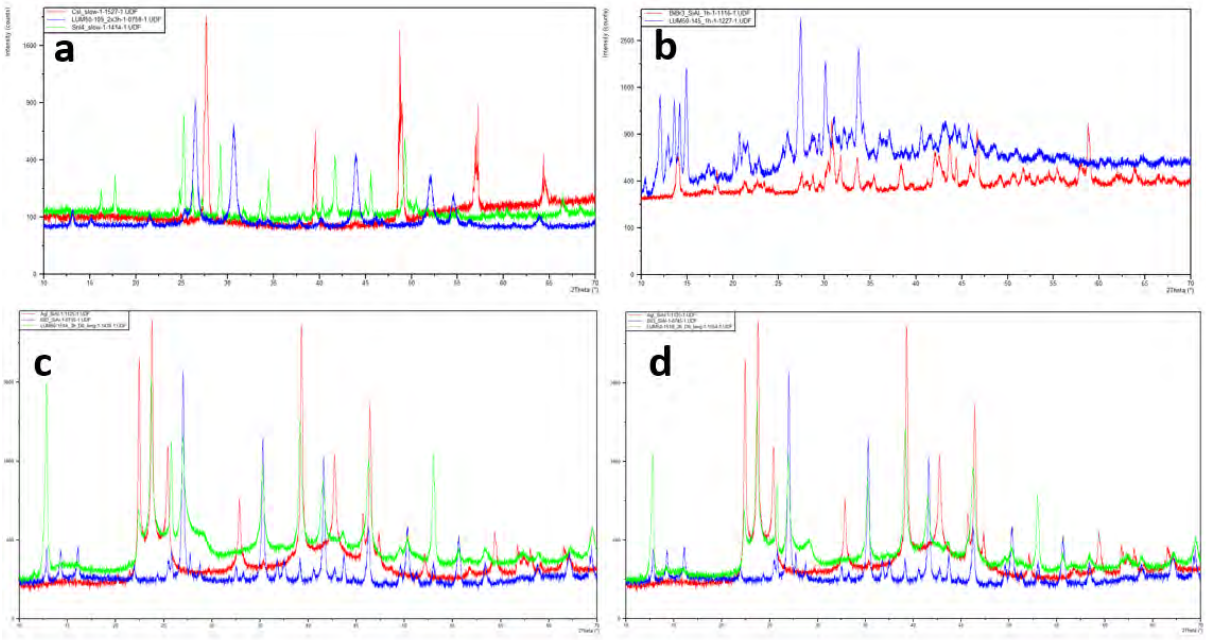

Figure 3.2.1-1. XRD Diffractogram of a) bulk Cs_2SnI_6 (blue) together with the raw materials (CsI - red, SnI_4 – green); b) bulk $FA_3Bi_2Br_9$ (blue) together with the raw material ($BiBr_3$ -red); c) bulk Ag_2BiI_5 (green) together with the raw materials (AgI – red and BiI_3 – blue) and d) Ag_3BiI_6 together with the raw materials (AgI – red and BiI_3 – blue).

The ball milling method applied by Avantama allows synthesizing any stable halide-based bulk LFP composition with minimum amount of competing phases. This approach can be extended to doped materials and enables the fast experimental screening. This property might be the key for further material tuning within the project. In the DropIT project Avantama has successfully developed and manufactured four types of LFPs, and will, if necessary, be able to develop further variants.

3.2.2 Synthesis of LFP nanocrystals by ball-milling

Ink formulations, based on different solvents, have successfully been developed from the different bulk LFP particle types in order to match the printability specifications of the ink-jet method (applied by UB) as well as spin coating / drop casting & general analysis (applied by UVEG). The inkjettable formulations contained nanoparticles with various loading and were optimized to show optimal viscosity, vapor pressure and surface tension as well as to show good chemical compatibility with the LFP nanoparticles. The whole consortium agreed to use dodecane as the inkjettable solvent. Table 3.2.2-1 shows the list of all samples sent to the partners (UB, UVEG, UJI).

Table 3.2.2-1. Samples of LFP nanoparticle dispersions distributed within the DropIT consortium

Sample Name	Particles	Solids load	Solvent	Partner
Cs_2SnI_6 Dispersion in Dodecane	Cs_2SnI_6	2.4%	Dodecane	UB, UJI
Cs_2SnI_6 Dispersion in Toluene	Cs_2SnI_6	2.4%	Toluene	UVEG
Ag_2BiI_5 Dispersion in Dodecane	Ag_2BiI_5	2.6%	Dodecane	UB, Saule

Ag_3BiI_6 Dispersion in Dodecane	Ag_3BiI_6	2.1%	Dodecane	UB, Saule
Ag_2BiI_5 Dispersion in Toluene	Ag_2BiI_5	2.2%	Toluene	UVEG, Saule
Ag_3BiI_6 Dispersion in Toluene	Ag_3BiI_6	1.8%	Toluene	UVEG, Saule

3.3 Synthesis and characterization of LFP nanocrystals CsBr:Sn

Flow-reactors are proficient for the preparation of nanomaterials under the continuous flow-rates of precursors, and the advancement is about their homogeneous mixing on ultrashort timescale and formation of nanoparticles. Herein, we used such flow-reaction method, see Figure 3.3-1, to prepare the ligand-free cesium tin bromide nanocrystals by a continuous flow of precursor solution and antisolvent. Two different flow pumps were connected with a common junction connected with a fixed length capillary tube. Dividing the volume of the capillary tube with the total flow-rates of two different flow pumps is known as residence time, calculated as the ratio Residence time = (Volume of capillary)/(total flow rate).

(a)

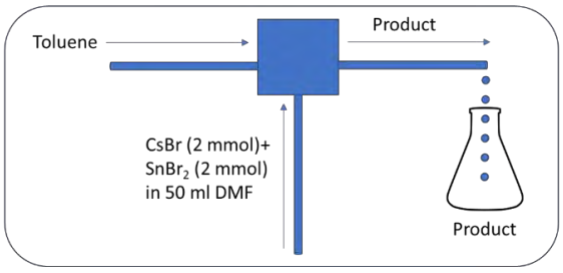

(b)

Entry	Flow_ Toluene (ml/min)	Flow_ Precursor (ml/min)
1	1	0.1
2	1	0.2
3	1	0.3
4	1	0.4
5	1	0.5

(c)

Figure 3.3-1. (a) Scheme of the flow reaction method. (b) Table of Set of samples prepared at different flow rates. (c) Digital image of our flow reactor system.

Herein, an equimolar ratio of CsBr and $SnBr_2$ was dissolved in a fixed volume of DMF, and stirred until to obtain a clear solution at room temperature. Toluene was used as the antisolvent. Flow rate of the antisolvent was fixed to 1 ml/min, and the flow rate of precursor solution was altered from 0.1 ml/min to 0.5 ml/min and studied the changes of the product. Figure 3.3-1a presents the scheme of our flow-reaction method as depicted above, and Figure 3.3-1b presents the table of a set of samples were collected under different flow ratio of precursor to the antisolvent. Figure 3.3-1c presents a digital image of the flow reactor system.

At low precursor flow-rates (0.1 and 0.2 ml/min), we observed an unstable green emitting material, which was lost its emission during the drying it to the powder. At the high precursor flow-rate (0.3-0.5 ml/min), we observed an orange emitting material, which was found to be stable over six months with the identical photoluminescence. We have characterized the X-ray diffraction (XRD) patterns for all the dried powder in open air, which is presented in Figure 3.3-2a. The XRD patterns of all of these samples were matched with CsBr (Pm-3m space group, cubic phase). The additional peaks were also observed at the low precursor to toluene ratio, which were belong to Cs_2SnBr_6 (mp-641923, triclinic phase). The unstable green emitting product was collected under the N_2, and it was coated with PMMA to protect it from the aerial oxidation. Figure 3.3-2b presents the XRD pattern of the PMMA-coated green emitting product, which matches with Cs_4SnBr_6 crystal phase. The aerobic instability of the green-emitting Cs_4SnBr_6 is due to the oxidation of Sn(II) to Sn(IV), and it transform to Cs_2SnBr_6 and CsBr. The XRD patterns for the samples prepared at low precursor to toluene ratio

only have the XRD pattern for Cs_2SnBr_6. Unfortunately, the intensities of those XRD peaks are very low in comparison to the CsBr because the low crystallinity of the oxidized product.

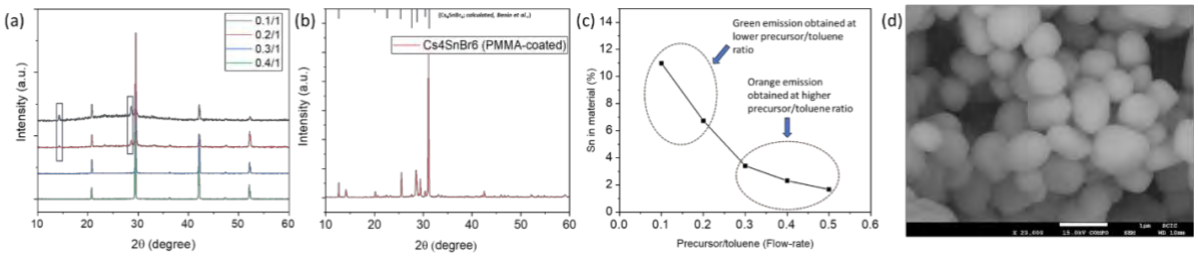

Figure 3.3-2. (a) XRD patterns of the dried powder samples prepared at different precursor to toluene flow rates. (b) XRD pattern of PMMA-coated air-unstable green emitting product at 0.1/1 precursor to toluene flow ratio. (c) Plot of elemental percentage of Sn present into the product vs precursor to toluene flow-rate. The percentage of Sn was calculated from the EDS measurements. (d) SEM image of Sn-doped CsBr synthesized at 0.4/1 precursor to toluene ratio.

At higher precursor to toluene ratio, we observe a phase pure CsBr XRD patterns, which is characterized as Sn-doped CsBr using other supporting characterizations (EDS and TGA, discussed later). We have characterized the elemental composition of Sn from the energy dispersive spectroscopy (EDS), and we found with increasing the precursor concentration, percentage of Sn was lost from the final material (Figure 3.3-2c, plot of % of Sn vs precursor to toluene ratio). With increasing the DMF content in the precursor solution, it used to dissolve more Sn present into the solution and a less portion of Sn is precipitated by incorporating into the CsBr crystal as a dopant at the interstitial site. Figure 2d presents the SEM image of Sn-doped CsBr prepared at higher precursor to toluene ratio (0.4/1), which shows the particle diameter is about 300-800 nm.

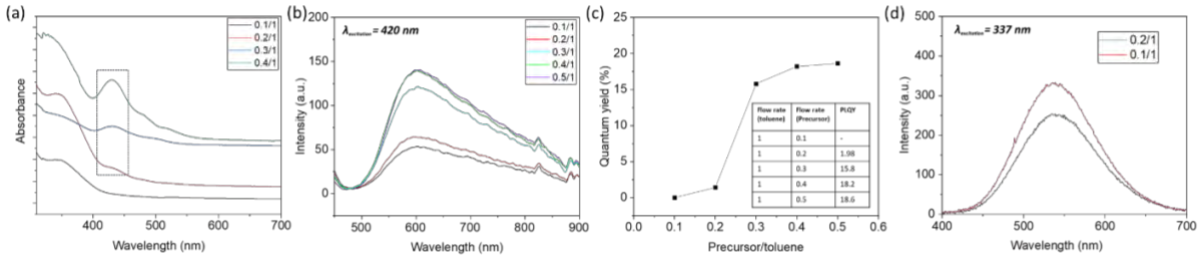

Figure 3.3-3: (a) Absorbance, (b) photoluminescence spectra and (c) PLQY of the dried powder samples prepared at different precursor to toluene ratio. PLQY values are presented in the inset of figure (c). The samples were excited at 420 nm for the measurement of PL and PLQY. (d) PL spectra of green emission obtained from the samples prepared at low precursor to toluene ratio, samples were collected under N_2. The excitation wavelength for the green emission was 337 nm.

The absorbance spectra of dried powder samples at different precursor to toluene ratio are presented in Figure 3.3-3a. At higher precursor to toluene flow-ratio, an absorbance peak near to 420 nm is observed, which is absent in 0.1/1, and a little hump in 0.2/1. At low precursor to toluene ratio, an absorbance peak is observed near 340 nm, which is similar to reported Cs_4SnBr_6 from the literature. Figure 3.3-3b presents a series of photoluminescence spectra of the aforementioned samples excited at 420 nm. The photoluminescence intensity increases at higher precursor to toluene ratio, and the corresponding PLQY data is also presented in Figure 3.3-3c. At higher precursor to toluene ratio, the PLQY was nearly 18%, which saturates further increasing the precursor to toluene ratio. The green emission obtained from the samples prepared at low precursor to toluene ratio is presented in Figure 3.3-3d. The excitation wavelength for the green emission is 337 nm.

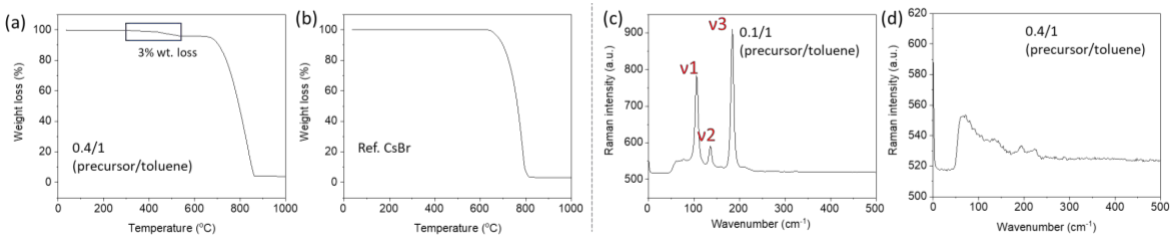

Figure 3.3-4. TGA plot of (a) Sn-doped CsBr prepared at higher precursor to toluene ratio, and (b) reference CsBr (precursor). RAMAN spectra at (c) 0.1/1 and (d) 0.4/1 precursor to toluene ratio.

Thermogravimetric analysis (TGA) was carried out to estimate the Sn-component into the material obtained at higher precursor to toluene ratio. Figure 3.3-4a presents TGA plot of 0.4/1 precursor to toluene ratio. From that plot, there is an initial 3% of weight loss near 320 °C, which belongs to the Sn-component into the material. Rest 97% decompose at higher temperature which corroborates well with the reference data of CsBr provided in Figure 3.3-4b. We have also performed RAMAN spectroscopy for the samples prepared at lower (0.1/1) and higher (0.4/1) precursor to toluene ratio, presented in Figure 3.3-4c,d, respectively. At low precursor to toluene ratio, there are three strong peaks observed, which are corresponding to the Br-Sn-Br asymmetric bending (v1), Br-Sn symmetric stretching (v2) and Br-Sn asymmetric stretching (v3) respectively. These all peaks belong to Cs_2SnBr_6 formed after the aerial oxidation of Cs_4SnBr_6. At higher precursor to toluene ratio, the asymmetric bending is absent and very low-intense peaks from the Sn-Br stretching vibration. This phenomenon can be tallied with TGA and EDS analysis, where we obtained very low percentage of Sn-dopant present into the structure at the higher precursor flow-rates.

The samples prepared at higher precursor to toluene ratio is characterized as the Sn-doped CsBr, which possess a phase-pure XRD pattern of CsBr, without having phase mixing related to any cesium tin bromide related component. This material has an outstanding photoluminescence with nearly 18% of PLQY belongs the Sn-dopant center which causes structural deviation upon the photoexcitation and hence creates the trapping of localized exciton, and furnish a broad self-trapped excitonic emission upon the excitation at 420 nm. The preparation of this material is carried out using the continuous flow-reactor with a high reproducibility. In addition, this material has a higher phase and optical stability over six months, and we found the same calculated PLQY from the same sample prepared six months earlier. Hence, Sn-doped CsBr could be consider as a next generation material for its optical performance and the stability.

3.4 Synthesis of $FAPb_{1-x}Sr_xI_3$ nanocrystals

We carried out the incorporation of different amount of Sr as a potential dopant into the $FAPbI_3$ perovskite quantum dots (PQDs), in order to provide red-emitting $FAPb_{1-x}Sr_xI_3$ materials with long-term stability and improved optical performance. By tracking the photophysical properties of the modified materials, we reached a photoluminescence quantum yield (PLQY) up to 100%, higher than that pure $FAPbI_3$, retaining the PLQY as high as 72% for 8 months after preparation. During the material characterization, we performed transmission electron microscopy (TEM) measurements to observe the morphology and the average particle size of PQDs in function of the Sr-doping level (4, 6, 7 and 12%). As shown in Figure 3.4-1a-e, we observed that PQDs show the typical nanocube shape, with a decrease in the particle size. The lowering of particle size has been associated to the high consumption iodide anions from the mixture reaction to mediate the growth and stabilization of the PQDs. Attending to the surface chemistry of PQDs, iodide species can passivate halide vacancies, while capping ligands such as oleylamine (in form of oleylammonium cations, OLAm) can substitute and fill some A-cation positions into the perovskite lattice. The replacement of a high fraction of A-cation sites by long alkylammonium chain such as OLAm is known as instant capping,

restricting the PQDs dimensions. Since Sr cannot substitute completely Pb positions into PQDs, Pb deficiency is promoted. Therefore, the stoichiometry of the reaction is altered, increasing both the oleylamine/Pb ratio and I/Pb into the mixture reaction.

On the other hand, the change in size is attended along with a modification in the optical properties of $FAPb_{1-x}Sr_xI_3$ PQDs colloidal solutions. Sr-doping blueshifts the photoluminescence (PL) peak of pure $FAPbI_3$ progressively (see Figure 3.4-1f and the Inset pictures in Figure 3.4-1a-e). Thus, it is deduced that Sr-incorporation induces quantum confinement effect (QCE) into PQDs. Interestingly, additional emission peaks were observed at lower wavelengths to surpass the Sr-doping level over 7 at.%, supposing the co-existence of diverse structures in the dispersion. As shown in Figure 3.4-1g,h, the TEM images reveal the emergence of nanoplatelets (NPLs), concluding that the abovementioned low-wavelength emission peaks are associated to this kind of morphology, also formed by altering the stoichiometry of reaction.

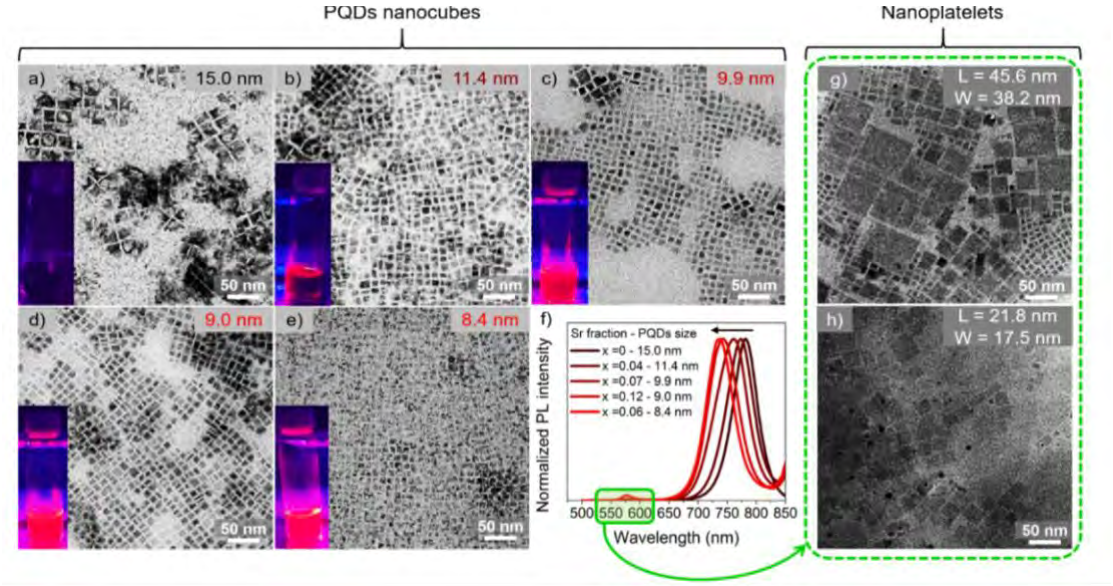

Figure 3.4-1. TEM images of (a) $FAPbI_3$ and $FAPb_{1-x}Sr_xI_3$ perovskite quantum dots (PQDs) colloidal solutions with (b) 4 at.%, Sr (c) 7 at.% Sr, (d) 12 at.% Sr and (e) 6 at.% Sr. (f) Photoluminescence spectra of the $FAPb_{1-x}Sr_xI_3$ PQDs colloidal solutions by varying the Sr fraction-particle size. TEM images of the (g) $FAPb_{0.88}Sr_{0.12}I_3$ and (h) $FAPb_{0.94}Sr_{0.06}I_3$ nanoplatelets (NPLs) from the redispersed precipitate by varying their corresponding lateral dimensions (L=length, W=width).

The high content of iodide anions in the mixture reaction by Pb deficiency is the needed source to facilitate the reduction of Schottky defects, which promotes the Sr^{2+}-doping. This fact can be observed in Figure 3.4-2a, which exhibit the increase of the PLQY (enhancement of radiative recombination, k_r), to reach the highest value after adding 7 at.% Sr. In this context, the non-radiative recombination (k_{nr}) channels provided mainly by Pb- and I- vacancies are reduced (Figure 3.4-2b), improving the optical features of the PQDs. Simultaneously, the straightening of the QCE given by the instant capping of PQDs increases the exciton binding energy, making faster the PL lifetime. Then, an excess of Sr provides the decrease of the PLQY, consequence of the strong Pb deficiency by incomplete Sr substitution. In this case, the free iodide content from the mixture reaction is consumed to form NPLs by alteration of the stoichiometry of the precursors, hindering the passivation of Schottky defects in the PQDs, and opening the door to the non-radiative recombination pathway for electron relaxation (higher k_{nr}/k_r ratio, See Figure 3.4-2c). At this point, it is deduced that the addition of 7 at.% into the $FAPbI_3$ PQDs maximize the suppression of structural defects and suppress the of non-radiative recombination mechanism, generating high-quality PQDs.

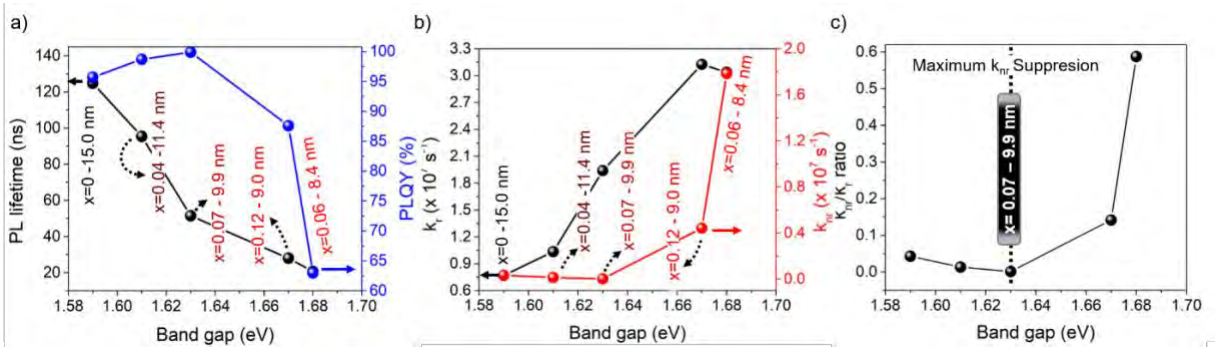

Figure 3.4-2. (a) Behavior of the PL lifetime and PLQY, (b) radiative (k_r) and non-radiative recombination (k_{nr}) decay rate constants and (c) their corresponding k_{nr}/k_r ratio for $FAPb_{1-x}Sr_xI_3$ PQDs colloidal solutions by varying the Sr fraction.

The PLQY of the synthesized samples was followed for 30 days under dark at room conditions, see Figure 3.4-3a, exposed to a high relative ambient humidity between 40-50%. As shown in Figure 3.4-3b, the PLQY of the $FAPbI_3$ PQDs continuously decreases after being practically null after 15 days. However, for samples containing Sr, the PLQY stabilizes after 3-6 days, preserving a value as high as 78% $FAPb_{0.93}Sr_{0.07}I_3$ PQDs after 30 days. The stability of the different PQDs under continuous UV illumination has also been analyzed, see Figure 3.4-3c. The PLQY of samples aged for 15 days at room conditions was tracked during 12 h under continuous UV illumination. We observed that the relative PL intensity increased for all the Sr-modified PQDs, associated to the photobrightening effect. Then, it is worth to highlight that $FAPb_{0.93}Sr_{0.07}I_3$ sample stored in the fridge (under dark conditions and 4 ºC) is stable for at least 8 months preserving a significant PLQY of 72%, see Figure 3.4-3d, with T_{80} = 6.5 months, where T_{80} is the time for which initial PLQY is reduced by 20%. Lastly, the Sr incorporation could boost the oxidizing power of PQDs for organic degradation (Figure 3.4-3e) or improve the chromaticity indexes near from the Rec. 2020 standards for red color (Figure 3.4-3f). These results indicate that Sr-PQDs are potential candidates to be applicable in solar-driven processes such as photocatalysis, and be part of competitive red light-emitting diodes.

The results of this work are under revision in a form of communication paper.

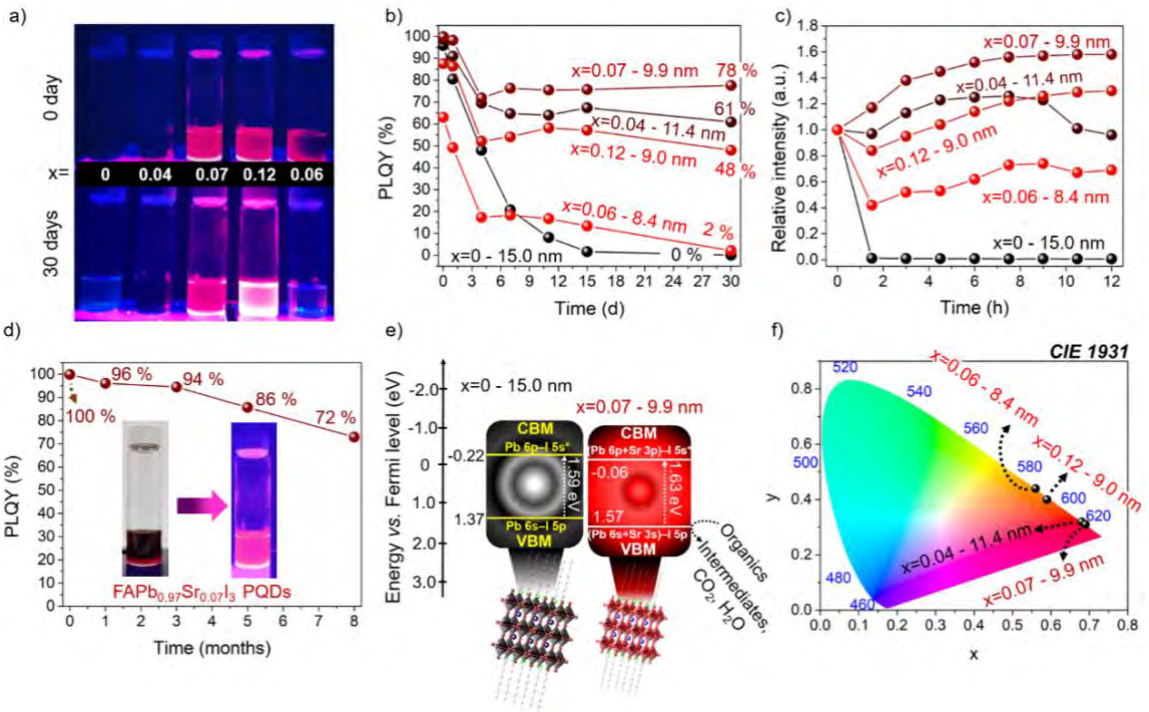

Figure 3.4-3. (a) Photographs of fresh and aged (after 30 days) $FAPb_{1-x}Sr_xI_3$ PQDs colloidal solutions under UV-light irradiation. (b) PLQY values as a function of aged days for PQDs colloidal solutions. (c) Photostability 15 days-aged PQDs exposed to UV light irradiation for 15 h. (d) PLQY stability of $FAPb_{0.93}Sr_{0.07}I_3$ PQDs colloidal solutions for 8 months, with T_{80} = 6.5 months. (e) Band structure of $FAPbI_3$ and $FAPb_{0.93}Sr_{0.07}I_3$ PQDs obtained from XPS VB spectra through the extrapolation method. (f) CIE chromaticity of Sr-substituted PQDs.

3.5 Synthesis of LFP thin films from molecular precursors

3.5.1 Preparation and Characterization of $CsSnI_3$ thin films

Lead halide perovskites boosted the solar cells efficiency in these last few years, up to 25.5%. Despite the outstanding optical and electrical properties, the most common organic-inorganic lead iodide perovskite materials has two main drawbacks, the stability and the toxicity of lead. The most obvious alternative is the replacement of the lead with the tin, in particular in the full inorganic $CsSnI_3$. There are a lot of possible lead-free candidates, but tin halide perovskites have drawn the attention of the scientific community, due to their similarities with the lead halide perovskites. The $CsSnI_3$ achieved 0.88% of efficiency in its first approach of a Schottky solar cell,[1] and with the inclusion of a 10% excess of SnI_2 in the formation of the film, or the 20% of SnF_2[2] to cover the tin vacancies, it achieved an efficiency around 2-2.76%. [3,4] Though the Sn (2+) easily oxidized in environmental conditions to the higher oxidation states (4+). After the oxidation a double perovskite Cs_2SnI_6 is formed, more stable than the no-oxidized counterpart. Although several synthesis methods have been employed for its preparation,[5,6,7] for the Task 1.4, **Cs_2SnI_6 film** has been obtained by the degradation and **reconstruction of the co-evaporated $CsSnI_3$ (Figure 3.5.1-1a,b,c)** and the corresponding powder by precipitation in solution (**Figure 3.5.1-1d**), methods selected in order to obtain a very pure material, to study its optical properties and compared them with the most common methylammonium lead iodide perovskite ($MAPbI_3$). The results highlight the potential of this material, not only regarding the stability, but also from the optical point of view. Furthermore the product of this work is a published paper in *ACS Appl. Energy Mater.* 2019, 2, 12, 8381-8387.

In order to evaluate the structural properties of the evaporated thin film material, the powder was synthesized as reference. In both cases we developed novel and easy methods. In the case of the thermal evaporation technique (the optimized temperature values for each crucible are: ~270°C for SnI_2 and ~510°C for CsI), we achieved the correct precursors (CsI and SnI_2) stoichiometry (1:1) in the final film, by calculating the deposition rate ratio, where the deposition rate of CsI must be 1.176 times bigger than the one of SnI_2 (Equation 1). It is, in fact, reasonable that the material volume ratio is proportional to the film thickness, and in turn to the evaporation rate. Thus, the volume ratio, depending on the molecular weight and densities (Equation 1) is equal to the rate ratio.

$$\frac{1\ mol\ CsI}{1\ mol\ SnI_2} \rightarrow \frac{259.81\ g\ CsI}{372.52\ g\ SnI_2} \rightarrow \frac{57.61\ mL\ CsI}{49\ mL\ SnI_2} = \frac{DepositionRate_{CsI}}{DepositionRate_{SnI_2}} = 1.176 \qquad (1)$$

The general consequence of this approach is that with this simple calculation, we can customize the ratio between the two precursors, and make films with CsI or SnI_2 excess, having different properties.[8] The obtained film has a uniform morphology, without pin-holes and low roughness, as shown in the Scanning Electron Microscopy (SEM) images (**Figure 3.5.1-1b, c**). The $CsSnI_3$ degradation and Cs_2SnI_6 reconstruction take between 3 and 5 days to get the film completely dark (**Figure 3.5.1-1e**), highlighting a certain stability of the evaporated $CsSnI_3$ in air, due to the high quality film obtained by evaporation, if compared with the spin-coated material reported in literature, which degraded and reconstructed in less 24h. On the other hand the Cs_2SnI_6 powder was synthesized by precipitation in solution, by mixing the precursor in acetone (**Figure 3.5.1-1d**). 1 mmol of CsI (259.81 mg) was mixed with 1 mmol of SnI_2 (372.52 mg) in a vial. 1mL of acetone was added

to the mixture to form a black suspension, gently stirred at 750 rpm for a couple of hours, in order to completely disperse the precursors. After the evaporation of the acetone in ambient conditions it was possible to collect the precipitated black crystals of Cs_2SnI_6. The X-Ray Diffraction (XRD) patterns of the powder and of the thin film are shown in **Figure 3.5.1-1f**. Here, we considered the powder as a reference pure material, with characteristic peaks at 13.16°, 26.52°, 30.72°, 44°, 52.04° and 54.68°, all of them representing lattice planes of Cs_2SnI_6.[8]

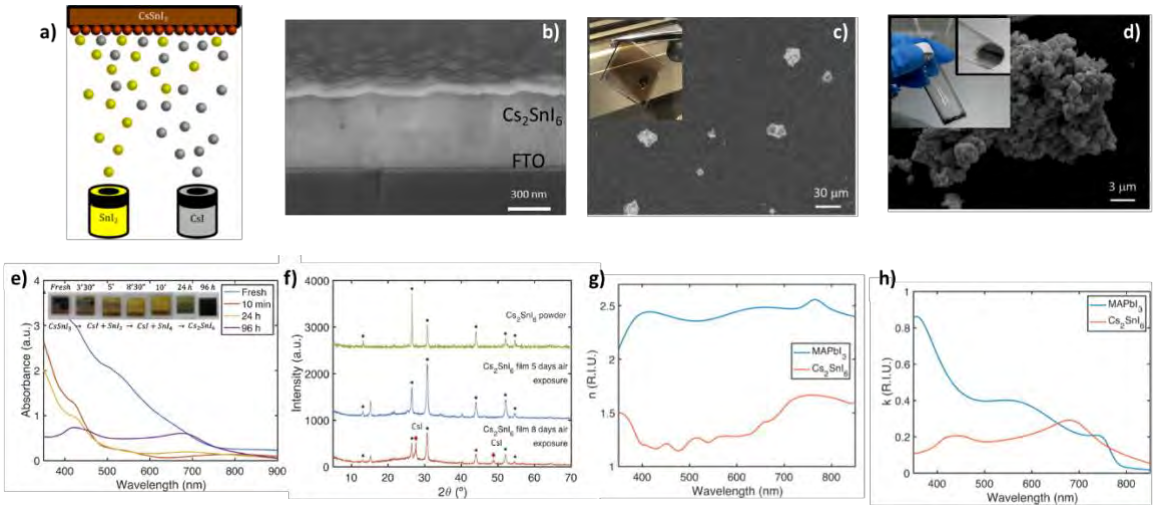

Figure 3.5.1-1 a) Scheme of the thermal co-evaporation fabrication process for the preparation of $CsSnI_3$; Scanning Electron Microscopy (SEM) images of **b)** cross section of the sample FTO/SnO_2/Cs_2SnI_6; **c)** Cs_2SnI_6 film; Inset: semitransparent $CsSnI_3$ film with a thickness of 230 nm (after 8 days on the SEM top view of the reconstructed Cs_2SnI_6, CsI crystals became visible, in accordance with the XRD in panel (f)) and **d)** pure powder sample (Inset: picture of the Cs_2SnI_6 pure powder). **e)** Absorbance decay due to $CsSnI_3$ degradation and absorbance recovery due to formation of Cs_2SnI_6 (Inset: picture of the degradation, oxidation of $CsSnI_3$ and reconstruction to the Cs_2SnI_6 thin film); **f)** XRD patterns of the pure powder and the thin-films of $CsSnI_3$ after 5 days and 8 days in air. After 5th day the $CsSnI_3$ film is totally converted in the Cs_2SnI_6. Black stars show Cs_2SnI_6 peaks, and red diamonds show the CsI peaks. **g)** Refractive index and **h)** extinction coefficient comparison between classical $MAPbI_3$ and Cs_2SnI_6 perovskite.

The absorbance spectra reported in **Figure 1c** show that the film recovers its capacity to absorb the wavelengths between 700 nm and 800 nm completely, but losing the absorption capacity in shorter wavelengths, and having a planar response with two humps, instead of the original ramp shape. This characteristic behavior, resulting in an average visible transmittance (AVT) of 42.1%, doubling the value of the AVT reported for 150 nm $MAPbI_3$ films,[9] is attractive for semitransparent application.[10] The optical properties of the Cs_2SnI_6 thin films prepared by degradation and reconstruction were systematically analyzed. We measured and calculated the absorption coefficient, band-gap, refractive index and extinction coefficient. The absorption, reflection and transmission of the films were measured, and the corresponding values were used to obtain the absorption coefficient, α, using the relation below: [11]

$$\alpha = \frac{1}{t} \cdot \ln\left[\frac{(1-R)^2}{T}\right] \approx 2.303 \cdot \frac{A}{t} \quad (2)$$

where, t is the thickness of the film, and R, T, A are Reflectance, Transmittance and Absorbance of the film. The approximation showed in Equation 2 is accepted if the reflectance is close to zero, as in this study. The values of refractive index and extinction coefficient, n and κ respectively, as a function of wavelength (λ), see Figure 1g,h, were obtained following Equation 3 and 4:[11]

$$\kappa = \frac{\alpha\lambda}{4\pi} \qquad (3)$$

$$n = \frac{-2(R+1) \pm \sqrt{\left(2(R+1)\right)^2 - 4(R-1)^2(1+\kappa^2)}}{2(R-1)} \qquad (4)$$

Two main aspects are remarkable here: the first one, regarding to n, is the huge difference between the $MAPbI_3$ (around 2.5) and the Cs_2SnI_6 (around 1.5). This fact can make Cs_2SnI_6 better than $MAPbI_3$ in terms of reflection and interface index matching, depending of the surrounding layers. The second important fact is regarding to κ, as $MAPbI_3$ can be considered a better absorber than Cs_2SnI_6, nevertheless, between 650 nm and 730 nm, Cs_2SnI_6 has a higher extinction coefficient that $MAPbI_3$, which implies that is a better absorber in this spectral interval. This fact points to a high potentiality of Cs_2SnI_6 for the development of photodetectors in this range.

With these results it is also possible to calculate the ideal short-circuit current density that a solar cell made with Cs_2SnI_6 could have. We have done this using the generation rate and supposing an ideal case with no electrical losses.[12]

$$J_{SC} = q \cdot \int_0^T G(x) \cdot dx$$

$$J_{SC} = q \cdot \int_0^T \int_{\lambda_{min}}^{\lambda_{max}} \frac{\lambda}{hc} \cdot Irr(\lambda) \cdot [1 - r(\lambda)] \cdot \alpha(\lambda) \cdot e^{-\alpha(\lambda)\cdot x} \cdot d\lambda \cdot dx$$

$$J_{SC} = \frac{q}{hc} \int_{\lambda_{min}}^{\lambda_{max}} \lambda \cdot Irr(\lambda) \cdot [1 - r(\lambda)] \cdot (1 - e^{-\alpha(\lambda)\cdot T}) \cdot d\lambda$$

Being q the electron charge, G(x) the generation rate, h the Planck's constant, c the speed of light, λ the incident wavelength in vacuum, α the absorption coefficient, T the thickness of the film, r the reflectance and Irr the irradiance value of the incident light.

From this equations, under the Sun spectrum (AM1.5G), we obtain a J_{SC} value of 18.86 mA/cm^2 in a device with an active layer thickness of 230 nm. The maximum value is obtained supposing ideal conditions (zero reflectance and an optimum optical thickness), and equals to 33.68 mA/cm^2.

This study demonstrates that Cs_2SnI_6 is a promising material for photo-devices, as it highlights its main characteristics and optical parameters, giving an original view on the use of the lead-free double perovskite, but at the same time emphasizing the need to improve the electrical properties for the development of efficient optoelectronic devices.

References

[1] Chen, Z.; Wang, J. J.; Ren, Y.; Yu, C.; Shum, K. *Appl. Phys. Lett.* **2012**, 101, 093901.
[2] Kumar, M. H.; Dharani, S.; Leong, W. L.; Boix, P. P.; et al. *Adv. Mater.* **2014**, 26 (41), 7122–7127.
[3] Koh, T. M.; Krishnamoorthy, T.; Yantara, N.; et al. *J. Mater. Chem. A* **2015**, 3 (29), 14996–15000.
[4] Marshall, K. P.; Walton, R. I.; Hatton, et al. *J. Mater. Chem. A* **2015**, 3, 11631-11640.
[5] Ke, J. C.-R.; Lewis, D. J.; Walton, A. S.; et al. *J. Mater. Chem. A* **2018**, 6, 11205-11214.
[6] Guo, F.; Lu, Z.; Mohanty, et al. *Mater. Res. Lett.* **2017**, 5, 540-546.
[7] Saparov, B.; Sun, J.-P.; Meng, W.; et al. *Chem. Mater.* **2016**, 28, 2315-2322.
[8] Song, T.-B.; Yokoyama, T.; Aramaki, S.; et al. *ACS Energy Lett.* **2017**, 2, 897-903.
[9] Masi, S.; Rizzo, A.; Munir, et al. *Adv. Energy Mater.* **2017**, 7, 1602600.
[10] Eperon, G. E.; Burlakov, V. M.; Goriely, A.; et al. *ACS Nano* **2014**, 8, 591-598.

[11] Hecht, E.; Zając, A. Optics. Addison-Wesley Pub. Co.: **1974**.
[12] Luque, A.; Hegedus, S. Handbook of Photovoltaic Science and Engineering, Wiley, **2003**.

3.5.2 Progress in the synthesis of Cs_2TiX_6 (X=Br or Cl)

Chemistry routes combined with self-assembly strategies have been used to prepare homogeneous thin films of polycrystalline novel Cs_2TiX_6 (X=Br or Cl) with the objective of create thin films deposited by spin coating, controlling the formation/growth and use them as benchmark materials for inkjet and device fabrication. To address the synthesis of this Pb-free PVK, we focused on the procedure reported in a previous publication (Joule 2018, 2, 1 – 13), where the material film is manufactured by CsBr evaporation and subsequent annealing of the Cs layer in a $TiBr_4$ atmosphere at 200ºC. That is, the synthesis is done by solid-state diffusion. The goal in this task is to synthesize lead free PVK based on environmentally friendly ions such as Cs^+ and Ti(IV), from stable Cs and Ti solutions, in order to create films and powders for inkjet technology, both of them by Soft Chemistry methodology, as shown in **Figure 3.5.2-1.**

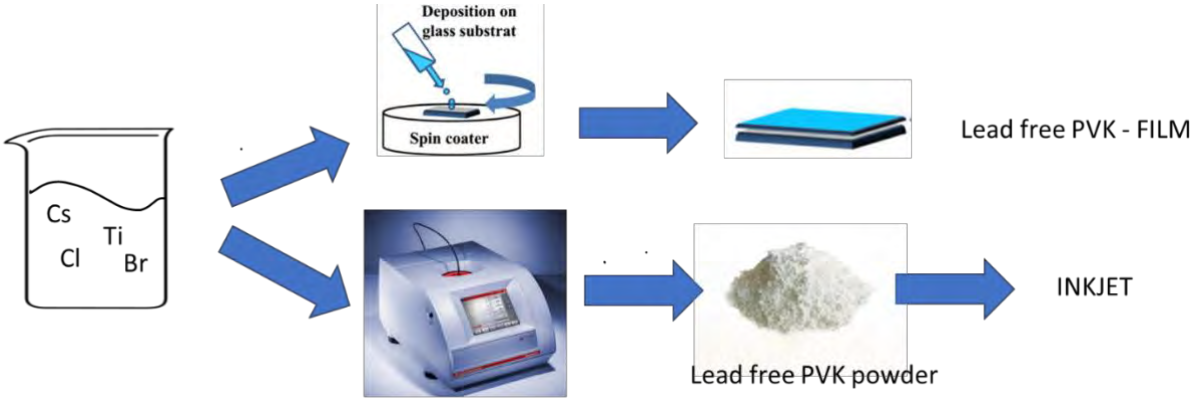

Figure 3.5.2-1. Schematic synthesis method to obtain film and powder of lead free PVK Cs_2TiX_6

Different solubility tests have been made of different Cs(I) and Ti (IV) precursors (chlorides, bromides) by using the stoichiometric Cs:Ti molar ratio. The most successful precursor has been $TiCl_4 \cdot THF$ complex (low sensitivity to moisture). The titanium complex was dissolved in EtOH, MeOH and DMSO; CsCl and CsBr were dissolved at molarity in different solvents (THF, DMF, DMSO).

The PVK Cs_2TiX_6 has been synthesized by two methods: (1) films by spin coating with Cs/Ti solutions of FTO substrates and annealing and (2) microwave synthesis with Cs/Ti solutions to obtain a Cs_2TiX_6 powder. Until now, the material has not been obtained with high homogeneity in films or in powder. In films, there are big aggregations and parts where the material is not well crystallized. On the other hand, the synthesis conditions for microwave method must be accurately adjusted, combining three parameters that play an important role in the synthesis, like time, temperature, and pressure, in order to avoid agglomeration.

For both methodologies, the main barrier has been the use of titanium in solution, due to its high tendency to precipitate as TiO_2 in moisture at ambient conditions. After this results we are currently focusing on new synthesis strategies, based on Trioctylphosphine oxide - TOPO (*J. Mater. Chem. C, 2017, 5, 10947)* for microwave method, were TOPO favors the dissolution of precursors and thus helps to get high-quality products. Thus, we expect to avoid large agglomeration by the use of this capping ligand. In addition, in the spin coating method, for perovskite films, a new strategy focused

on the development of a fast and controllable crystallization of perovskite films by microwave irradiation process (*ACS Appl. Mater. Interfaces 2016, 8, 7854−7861)* is planned. In comparison with the conventional thermal annealing process, a microwave irradiation process assisted fast and controllable crystallization of perovskite films with less energy-loss and time consumption and therefore resulted in the enhancement in the photovoltaic performance of the corresponding solar cells.

4 Conclusions & Future directions …

Results can be summarized for two subgroups of materials.

4.1 Benchmark $FASnI_3$ colloidal nanocrystals

- Nanocrystals with nearly the best possible morphological quality and purity have been developed
- Disorder of the I-sites has been discovered for the synthesized $FASnI_3$ NCs
- Despite the absence of Sn^{4+} states, the QY of $FASnI_3$ NCs is low (~0.5 %), likely due to disorder
- Lattice distortions by doping have been tested as possible way to increase QY
- The most important issue of $FASnI_3$ NCs is related to their low oxidative stability which requires storage and processing in inert atmosphere
- Possibility to improve stability by altering A-site cation and/or admixing reducing agents will be explored
- The manuscript describing the synthesis and properties of colloidal $FASnI_3$ NCs is in preparation
- According to literature $FASnI_3$ remains to be the most efficient LFP material for the photovoltaics. It is yet unclear whether device manufacturing from colloidal NCs is beneficial compared to molecular precursors or not. Therefore work in both directions will continue, mainly towards improving stability of this material

4.2 Alternative LFP materials

- Series of the alternative LFP materials have been investigated
- Sb-doped double perovskites and Sn-doped CsBr exhibit intense (PL QY 20-90 %) photoluminescence in visible range allowing to consider these materials for lightening and remote thermography applications
- Vacancy-ordered Cs_2SnI_6 and $Cs_3Bi_2I_9$ NCs may be considered as photodetectors in visible range
- New materials predicted computationally (Cs_2ZrI_6) will be synthesized and characterized